Vacancy doping and charge transport in Bi_2S_3 nanoparticle films for photovoltaic applications

Jan Mock,[1] Benjamin Klingebiel,[1,*] Diana Schillings,[1] Maurice Nuys,[1] Jan Flohre,[1] Shuo Wang,[1] Thomas Kirchartz,[1,2] and Reinhard Carius[1]

[1]*IEK5-Photovoltaik, Forschungszentrum Jülich, 52425 Jülich, Germany*

[2]*Faculty of Engineering and CENIDE, University of Duisburg-Essen, Carl-Benz-Straße 199, 47057 Duisburg, Germany*

(Received 30 May 2018; revised manuscript received 14 August 2019; published 21 October 2019)

Native point defect doping via thermal treatment is an easy and promising method to tune the electrical transport properties of semiconductors made for renewable-energy conversion. In this study, we investigate the vacancy doping of the lowly toxic semiconductor Bi_2S_3 using electrical conductivity as well as thermoelectric power measurements. We enhance the electrical conductivity of bismuth sulfide nanoparticle layers by more than four orders of magnitude by a stepwise thermal treatment in a moderate temperature range (300–480 K). Via thermoelectric power measurements we attribute this enhancement to an increase in charge-carrier mobility by two orders of magnitude and to an increase in charge-carrier density by more than two orders of magnitude. We find that the energetic position of the electron-doping sulfur vacancies of bismuth sulfide nanoparticles is significantly shallower than previously reported for bulk material. Subsequently, we implement Bi_2S_3 nanoparticles doped with sulfur vacancies by thermal annealing in photovoltaic devices using P3HT as an electron donor molecule. We find that annealing up to 383 K yields the best compromise between improving charge-carrier transport and increasing defect densities.

DOI: 10.1103/PhysRevMaterials.3.105406

I. INTRODUCTION

Over the past years, hybrid organic-inorganic solar cells have received increasing attention. These devices combine the potential for solution processability and high absorption coefficients of organic and nanoparticular materials with the expectation to provide improved charge transport in the inorganic part of the hybrid systems as compared to purely organic materials [1–5]. While there exists a large variety of organic semiconductors which have been used for photovoltaic applications, there is so far a quite limited number of inorganic solution-processable materials that could be used in hybrid solar cells and other electronic and optoelectronic devices. Recent years have seen a strong focus of research on lead-halide perovskite based thin films [6,7], but both stability [8–11] and the toxicity of lead and tin are of some concern [12,13]. While also many of the solution-processable inorganic absorbers based on nanoparticles contain Cd or Pb sulfides or selenides [14–16], there have been a few approaches to use nanoparticles with a low toxicity of the constituting elements such as Bi_2S_3 [17–23]. One of the peculiar properties of Bi_2S_3 is that in addition to its low toxicity [24,25], the material is *n* type, while most other nanoparticle-based absorber materials such as PbS are *p* type [17].

In hybrid solar cells Bi_2S_3 nanoparticles in combination with a photon-absorbing and electron-donating polymer can be used as the electron-accepting material [26]. Apart from suitable energy levels to accept the electrons and block holes, one requirement for Bi_2S_3 as an electron-accepting and electron-conducting material is to have a sufficient electron mobility to achieve efficient charge transport to the contact [27,28]. Furthermore, based on the band gap of around 1.4 eV of Bi_2S_3 and the fairly high absorption coefficient, Bi_2S_3 has the potential to contribute to the photocurrent by itself [22]. Thus, investigating and enhancing the charge-carrier mobility of Bi_2S_3 nanoparticle layers is desired to improve the overall performance of these hybrid solar cells.

Deviation of the stoichiometric composition is commonly undesired and therefore one tries to avoid it in most cases. However, the intentional tuning of a tiny stoichiometric deviation is a powerful method to enhance the electrical transport properties of semiconductors [29]. Native defect doping is already applied for a variety of semiconducting metal oxides in the field of energy conversion and storage [30,31]. However, the same approach can be applied for metal sulfides [32], bismuth sulfide in our case. While charge transport in Bi_2S_3 has been investigated extensively in the context of applications for thermoelectrics with a variety in material morphology (e.g., bulk [33], polycrystalline [34–37], nanowire [38], and nanorods [39,40]), there has been no detailed study on nanoparticles so far. The literature provides evidence of enhanced electrical conductivity via native point defect doping of sulfur-deficient bismuth sulfide (Bi_2S_{3-x}) [34,38,41–43]. Sulfur vacancies act as electron donors and therefore increase the charge-carrier density. Sulfur vacancy doping of bismuth sulfide has already been applied for thermoelectric applications, but as far as we know, has not been studied in detail for photovoltaic applications.

This work is structured in two parts. In the first part, we study the electrical transport properties of bismuth sulfide nanoparticle layers with a combination of electrical conductivity measurements as well as thermoelectric power measurements while annealing under vacuum conditions. With this combination we are able to investigate doping via sulfur vacancies and also determine the charge-carrier mobility

*Corresponding author: b.klingebiel@fz-juelich.de

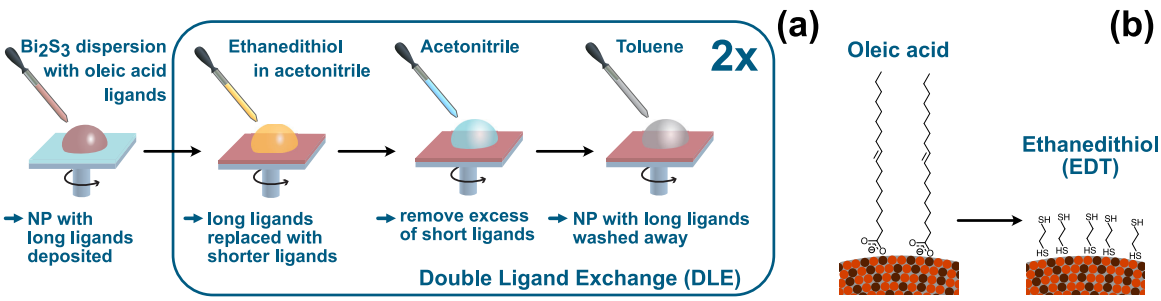

FIG. 1. (a) Schematic drawing of the layer-by-layer ligand exchange. In the first step the nanoparticles (NPs) are deposited, which are stabilized by oleic acid. During the second step, the oleic acid is replaced by the shorter ligand ethanedithiol (EDT). Steps three and four remove the excess of EDT and NPs that did not perform the ligand exchange. Steps two to four are repeated twice to ensure a complete ligand exchange. (b) Schematic drawing of the ligands oleic acid and EDT.

within the nanoparticle layer. We show electrical conductivity as well as thermoelectric power measurements of Bi_2S_3 nanoparticle layers under stepwise annealing with increasing temperatures from 300 K up to 475 K. We present a method to enhance the electrical conductivity continuously by more than four orders of magnitude by annealing under vacuum conditions. Via thermoelectric power measurements we can separate the contribution of an increased charge-carrier density by more than two orders of magnitude and an enhanced electron mobility by two orders of magnitude. In the second part, we show solar cells in which bismuth sulfide nanoparticles are combined with the electron-donating polymer poly(3-hexylthiophene) (P3HT). We study the influence of the sulfur vacancy doping in these solar cells. We find an optimal annealing temperature of 383 K that increases the short-circuit current by 1 mA/cm². Annealing with higher temperatures reduces the open-circuit voltage caused by too many introduced sulfur vacancies acting as recombination centers. We combine our results from the transport studies and the device studies in the end of the second part.

II. METHODS

A. Nanoparticle synthesis

Bismuth sulfide nanoparticles were synthesized based on the hot injection method described elsewhere in detail [17,44,45]. In short, $Bi(CH_3COO)_3$, oleic acid, and 1-octadecane (ODE) were evacuated over night at 100 °C. The temperature was raised to 170 °C and bis(trimethylsilyl)sulfide solved in ODE was rapidly injected, which caused the solution to turn black immediately. The temperature was decreased and kept at 100 °C for two hours. The temperature was rapidly decreased by the addition of 20 ml cold octane and 40 ml methanol. Afterward the dispersion was centrifuged and washed in several steps with acetone and toluene under inert atmosphere. In the end the nanoparticles were dispersed in octane.

Thereby we synthesized nanoparticle with a flakelike shape with dimensions of several nanometers thickness and about 20 nm width. From these dimensions compared with the literature we exclude any significant quantum confinement effects, e.g., on the band gap [21,45,46].

B. Sample preparation

Bismuth sulfide (Bi_2S_3) nanoparticles were synthesized with oleic acid as a ligand to stabilize the nanoparticle dispersion. To improve charge transport between the nanoparticles we replace the approximately 2.5 nm long oleic acid ligands by ethanedithiol, which is around 0.5 nm long. To achieve homogenous layer formation of Bi_2S_3 nanoparticles, we adapted the concept of Martinez *et al.* to perform a layer-by-layer ligand exchange [40]. The routine is depicted in Fig. 1, where the nanoparticles are deposited in the first step by spin-casting the nanoparticle dispersion, which is stabilized by the long oleic acid ligand and solved in toluene. We perform ligand exchange by following three steps: The shorter ligand ethanedithiol (EDT), which is solved in acetonitrile, is spin coated to replace the oleic acid. Afterward the excess EDT gets washed away by spin-coating the solvent acetonitrile. In the last step we spin-coat toluene to remove the excess oleic acid as well as nanoparticles which did not perform the ligand exchange. By repeating the ligand exchange cycle two times, further referred to as double ligand exchange (DLE), we were able to increase the charge-carrier mobility and therefore the electrical conductivity by three orders of magnitude (shown in Fig. S1 of the Supplemental Material [47]) compared to nanoparticle layers which underwent only one ligand exchange cycle in between the nanoparticle deposition.

For scanning electron microscopy (SEM) imaging of pristine nanoparticles, aluminum-doped zinc oxide (ZnO:Al) as a conductive substrate was used instead of insulating quartz glass. After annealing, the bismuth sulfide nanoparticle layer was conductive enough to perform SEM imaging. As depicted in Fig. 1, the nanoparticle dispersion is stabilized after synthesis with oleic acid as a ligand. To achieve a homogeneous nanoparticle layer formation whereby the (long) ligand oleic acid is exchanged by a shorter ligand, a solution of 1,2-ethanedithiol in acetonitrile (2% v/v) is spin coated on top of each Bi_2S_3 layer.

C. Electrical conductivity and thermoelectric power

The electrical conductivity as well as the thermoelectric power measurements are based on Ref. [48]. The setup consists of a vacuum chamber with a gas inlet for different atmospheres (e.g., synthetic air, nitrogen). Under vacuum conditions, a vacuum base pressure between 3×10^{-7} and

10^{-6} mbar can be achieved. The sample is thermally contacted with silver glue on a sapphire glass holder, which is connected to two independent heaters (see Fig. S2 of the Supplemental Material [47] for more details). For electrical contact as well as for determination of the sample temperature, two 50 μm thin type-E (NiCr/CuNiMn) thermocouples are glued on the surface of the investigated material. Usually, two 8 mm wide coplanar metal (Au) contact stripes with a distance of 4 mm are evaporated on the samples. Considering the contact geometry and the layer thickness, the electrical conductivity is determined by applying 100 V (linear response regime in terms of the sample resistance) to the sample and measuring the resulting current by a Keithley 617 electrometer. The nanoparticle layers investigated in this work exhibited an absolute resistance in between the order of 10^6 and 10^{10} ohms. Thus, contact resistances are neglectable and a 2-terminal contact configuration is sufficient for electrical studies.

The thermovoltage is determined by applying a temperature gradient of 60 K at the heaters, which results in a temperature gradient of circa 15 K between the metal contact stripes on the sample. To determine the Seebeck coefficient $S(T)$ (thermoelectric power) the temperature gradient is applied successively with a positive and negative sign around the average sample temperature T. The measured thermovoltages were fitted linearly and the determined slope of the fit corresponds to the thermoelectric power. The setup was cooled with liquid nitrogen to achieve temperature gradients around room temperature.

The charge-carrier density n is calculated from the thermoelectric power. Therefore, a temperature-dependent effective density of states $N_C(T)$,

$$N_C(T) = 2\left(\frac{2\pi\ m_{\text{eff}} kT}{h^2}\right)^{3/2}, \tag{1}$$

where k is the Boltzmann constant and h the Planck constant, was assumed for n-type Bi_2S_3 to be $2.17 \times 10^{15} T^{3/2}$ cm^{-3}, which corresponds to an effective electron mass m_{eff} of 0.587 electron masses [33]. Furthermore, ionized defect scattering was assumed as the dominant scattering mechanism for the charge-carrier density calculation, which leads for a nondegenerated semiconductor to the expression of the thermoelectric power:

$$S(T) = -\frac{k}{e}\left\{\frac{4F_3[\epsilon^*(T)]}{3F_2[\epsilon^*(T)]} - \epsilon^*(T)\right\}, \tag{2}$$

where $\epsilon^*(T) = \frac{E_F - E_C}{kT}$ is the reduced Fermi energy (with E_F as the Fermi level and E_C as the conduction band edge), e is the elementary charge, and F_x is the Fermi-Dirac integral. In this work we apply the model of charge-carrier dynamics developed for polycrystalline thin films with (severe) potential fluctuation at grain boundaries [49] on our nanoparticular thin films. Thus, we transfer the grain boundary scattering mechanism (i.e., dominant scattering on ionized defect) on the inter-nanoparticle contacts. Furthermore, because the morphologies of the investigated samples are changing from nanoparticle layers toward nanocrystalline thin films during our measurement routine, we adopt the described scattering mechanism on both regimes to avoid discontinuity within our results.

To calculate the charge-carrier density, Eq. (2) is solved for $\epsilon^*(T)$ and inserted into

$$n(T) = N_C(T)\, F_{1/2}[\epsilon^*(T)], \tag{3}$$

with the effective density of states as mentioned above. By including the electrical conductivity σ, the charge-carrier mobility μ can be calculated with the well-known dependency

$$\sigma(T) = e\, n(T) \mu(T). \tag{4}$$

With this, the assumed effective density of states affects n and μ linearly, which is again affected by the effective electron mass. As an example, for a two times higher effective electron mass the calculated charge-carrier density would be $2^{3/2}$ times smaller and the mobility $2^{2/3}$ times higher. Therefore, the determination of the absolute values of n and μ from thermoelectric powers is based on the knowledge of the dominant scattering mechanism and the effective electron mass. But, relative changes of n and μ remain meaningful, as long as the dominant scattering mechanism and the band structure do not change significantly upon annealing.

D. Scanning electron microscopy

The microscope used was a Zeiss (Leo) Gemini 1550, that has a Schottky field-emission cathode and an in-lens detector. The lateral resolution equals around 1 nm at 20 kV and the measurement was performed under a vacuum base pressure of 10^{-6} mbar.

E. Raman spectroscopy

Raman measurements under ambient conditions were performed with a cooled silicon CCD adapted to a single-grating monochromator. The excitation was done with a 532 nm semiconductor laser (Coherent sapphire). The spectral resolution of the setup was 1.1 cm^{-1} (wave number).

F. Photothermal deflection spectroscopy

Bismuth sulfide nanoparticles were spin coated (with the ligand exchange following the DLE routine) on a quartz glass substrate in a glove-box environment as described before. Photothermal deflection spectroscopy (PDS) was used as a highly sensitive technique to obtain the absorptance of bismuth sulfide nanoparticle layers in a dynamic range of several orders of magnitude. A detailed description of this method can be found elsewhere [50,51]. The sample is measured in a cuvette filled with a CCl_4 solution, which is chemically inert and exhibits a temperature-dependent refractive index. A halogen lamp (100 W) in combination with a spectrometer (270 m from Horiba Jobin Yvon) illuminates the sample with monochromatic light in transverse mode. Any absorbed photon energy by the sample will eventually be converted into heat, which is released to the surrounding media. A probe beam from a diode laser (650 nm), adjusted in parallel to the sample surface, will be deflected due to the gradient in the refractive index of the chemical. Finally, the deflection angle, monitored by a silicon four-quadrant diode, is directly proportional to the power of the absorbed light. The samples were annealed with different annealing temperatures in an inert glove-box environment on a hot plate, where the sample temperature

was determined with a glued-on 50 μm type-E thermocouple. The samples were handled exclusively under inert conditions in between the measurement and the annealing. To determine the absorption coefficient, the PDS signal was normalized to its maximum, which corresponds to the absorptance of the nanoparticle layer. Furthermore, the time delay between the PDS signal from the thin nanoparticle layer and the thick substrate was used to reduce the contribution of the background absorption of the quartz glass substrate. Afterward, an effective nanoparticle layer thickness was approximated to match the absorption coefficient given in the literature [52]. The deduced layer thicknesses were between 85 nm and 120 nm.

G. Device fabrication

Devices were prepared on 12×12 mm^2 pre-patterned glass/ITO (150 nm) substrates from Psiotec Ltd., UK. For the ZnO contact layer a 0.46 mol/l solution of zinc acetate dihydrate and 0.42 mol/l ethanolamine in methoxyethanol were spin coated at 3000 rpm for 40 s and dried for 30 min on a hot plate at 200 °C under ambient atmosphere. The process was repeated twice to reach a thickness of around 50 nm. After the substrates were transported to a N_2 atmosphere glove box ($O_2 < 1$ ppm), the Bi_2S_3 nanoparticle layer was spin coated using the DLE procedure, which was repeated twice to reach an effective layer thickness of about 50 nm. After the annealing step (between room temperature and 160 °C) a solution of P3HT (Ossila Ltd., UK, 30 mg/ml in dichlorobenzene) was spin coated at 9000 rpm for 120 s and again annealed for 15 min at 100 °C. This results in a layer thickness of about 80 nm. For the hole-selective contact and the back contact molybdenum oxide (MoO_x, 30 nm, 0.2 Å/s) and silver (200 nm, 2 Å/s) were thermally evaporated in a Lesker Mini Spectros system attached to our glove box. This was done using a shadow mask to define six cells with an area of six times 0.06 mm^2.

H. *I-V* measurements

Standard illuminated and dark *I-V* measurements were performed with a setup integrated into our glove-box system consisting of a white-light LED source (Cree Inc. 100 W, 3680 lm) and a Keithley 2450 source measurement unit, which is connected via a 4-terminal configuration with the solar cell samples (see Fig. S3 of the Supplemental Material [47]). The light intensity of the LED was calibrated to the same short-circuit density measured with a representative Bi_2S_3/P3HT solar cell at an AM1.5G solar simulator. The setup was also used for dark *I-V* measurements to determine the series resistance R_S, parallel resistance R_P, diode ideality factor n_{id}, and dark-current density J_0. This was done by fitting the following diode equation to the dark *I-V* data [53]:

$$J = J_0\left\{\exp\left[\frac{q(V - JR_S)}{n_{id}k_BT} - 1\right]\right\} + \frac{V - JR_S}{R_P}. \quad (5)$$

I. Fourier transform photocurrent spectroscopy

The Fourier transform photocurrent spectroscopy (FTPS) setup is described in detail elsewhere [54]. In short a Bruker Vertex 80v UV/VIS/FTIR spectrometer combined with a Femto DLPCA-200 current-voltage amplifier is used to measure the wavelength dependence of the photocurrent for photon energies between 0.5 eV and 3 eV with a very high dynamic signal range. To calibrate the measurements to an external quantum efficiency (EQE) scale, the photocurrent is also measured while the cell is illuminated with a HeNe laser with a spot size of about 1 mm^2 centered on the active area and a power of 100 μW (measured with a Coherent LM-2). The FTPS raw data are then linearly scaled so that the QE measured with the laser is reached at 633 nm.

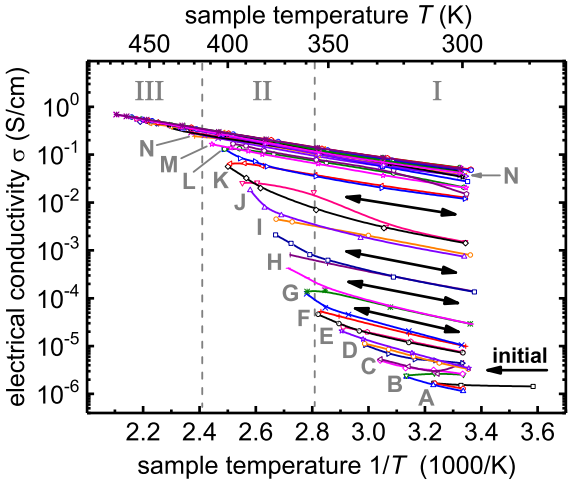

FIG. 2. Arrhenius plot of the electrical conductivity of a layer of ligand-exchanged Bi_2S_3 nanoparticles. The sample was stepwise annealed up to increasing temperatures (A to N). After each annealing step, the sample was cooled down to room temperature. Therefore, the initial electrical conductivity at 300 K was enhanced from 10^{-6} S/cm up to 5×10^{-2} S/cm by annealing up to 475 K under a vacuum base pressure of around 10^{-7} mbar.

III. RESULTS

A. Electrical conductivity and thermopower measurements

As described in the introduction, sulfur vacancies increase the charge-carrier density of bismuth sulfide and therefore enhance the electrical conductivity. We want to generate these sulfur vacancies via thermal annealing with a stepwise increasing temperature under vacuum conditions. Simultaneously to this stepwise annealing we determine the electrical conductivity as well as the thermoelectric power (Seebeck coefficient) to examine the charge-carrier density and the charge-carrier mobility.

Figure 2 shows an Arrhenius plot of the electrical conductivity of circa 8 to 10 monolayers (around 250 nm) of ligand-exchanged Bi_2S_3 nanoparticles. The sample was stepwise annealed up to a certain maximum temperature and then cooled down to room temperature afterward. This cycle was then repeated with a higher maximum temperature and each cycle was labeled with a capital letter (A to N) with A indicating the lowest maximum temperature T_{max}. After the annealing steps A to N, the electrical conductivity is enhanced and exhibits metastable conductivity levels (indicated by black arrows) while cooling down to room temperature. By annealing up

to 415 K the electrical conductivity at room temperature is raised by more than four orders of magnitude from 10^{-6} S/cm up to 5×10^{-2} S/cm (indicated as temperature regions I and II) and does not increase further while annealing up to 475 K (region III). For annealing temperatures above 545 K the Bi_2S_3 nanoparticles decompose as expected from Refs. [27,55], which is shown in Fig. S1.

To examine the charge-carrier density and mobility, we also determined the thermoelectric power during this annealing routine (shown in Fig. S4 of the Supplemental Material [47]), which reveals an *n*-type behavior of Bi_2S_3 for all annealing conditions used in this paper. Similar results for the thermoelectric power are also found for other Bi_2S_3 nanomaterials [39,56]. However, our mobilities are considerably lower. For better clarity, we will further plot the determined values against the maximum annealing temperature T_{max} (comparable with A to N).

In the following we want to distinguish between the contributions to the enhanced conductivity of the generated sulfur vacancies and the influence on the charge-carrier mobility. In addition, we want to determine whether there is a correlation between both values. This correlation is expected for example by the Seto model for polycrystalline semiconductors [49]. Therefore, first we want to introduce the sulfur vacancies and afterward reduce the sulfur vacancy concentration by the introduction of oxygen. Thus, we performed the whole annealing routine for an eight-times spin coated Bi_2S_3 DLE layer twice with a synthetic air flush at room temperature in between. Figure 3 presents the results of these experiments with the solid lines representing the initial run and the dashed lines representing the second run after the atmospheric flush.

In the following we will study two main features of the results: First, up to an annealing temperature of 356 K the charge-carrier mobility [depicted as red solid line in Fig. 3(b)] remains approximately at the initial value of around 10^{-3} $cm^2/(Vs)$, which is indicated as temperature region I. During the annealing in region II, the charge-carrier mobility increases up to 10^{-1} $cm^2/(Vs)$ and remains at this maximum value in region III. In contrast, the charge-carrier density increases from its initial value of 10^{16} cm^{-3} during the whole annealing in regions I and II up to its maximum value of 3×10^{18} cm^{-3}. The second feature is that after the introduction of dry synthetic air ($20\%\,O_2 + 80\%\,N_2$ at 0.8 atm) at room temperature, the charge-carrier density drops to roughly the initial value but the charge-carrier mobility stays almost the same. We interpret this behavior as being caused by two effects: The introduction of sulfur vacancies (Bi_2S_{3-x} with rising x), which act as electron donors, increases the charge-carrier density [33,34]. We emphasize that sulfur vacancies of bismuth sulfide can only act as electron donors in contrast to other semiconducting metal sulfides, e.g., cupper sulfide [32,41]. Those sulfur vacancies can be passivated by the introduction of oxygen atoms, which results in a reduced charge-carrier density ($Bi_2S_{3-x}O_x$). It is worth mentioning that the charge-carrier density after the second run exhibits a lower maximum value of 2×10^{18} cm^{-3}. This maximum doping concentration will be discussed later in this paper.

The observation of the enhanced charge-carrier mobility can be attributed to a changed morphology of the nanoparticle layer, which is not reversible under atmospheric changes. The

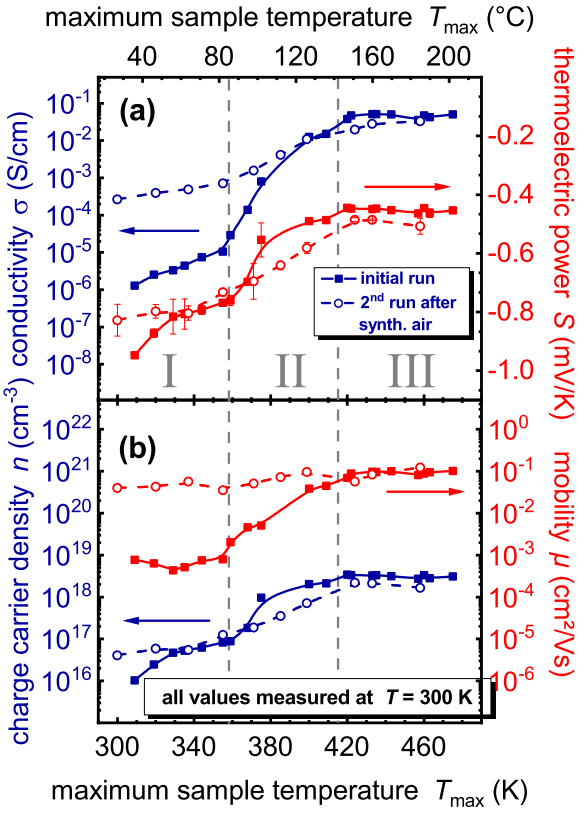

FIG. 3. Electrical conductivity, thermoelectric power, charge-carrier density, and charge-carrier mobility at 300 K as a function of the annealing temperature T_{max} of around 10 monolayers of Bi_2S_3 nanoparticles at a vacuum base pressure of around 10^{-7} mbar. The initial stepwise annealing series is depicted as solid lines. After annealing up to 475 K, the sample was cooled down to room temperature and dry synthetic air ($20\%\,O_2 + 80\%\,N_2$ at 0.8 atm) was introduced. Afterward, the annealing series was performed again (dashed lines). The region I (300–356 K) indicates the temperature range where the electrical conductivity is mainly rising because of increased charge-carrier density. In region II (356–415 K) additionally the mobility rises by about two orders of magnitude and in region III (415–545 K) all values remain constant.

SEM images shown in Fig. 4 support this explanation, where the nanoparticles are (b) separated directly after the deposition and (c) sintered after annealing up to 475 K.

To have an even closer look at the charge-transport properties, we determined the thermal activation energy E_σ of the temperature dependence of the electrical conductivity. The activation energy E_σ is defined as the slope of the metastable conductivity levels of Fig. 2. Because the activation energy E_σ of the conductivity consists of the activation energy E_n of the charge-carrier density as well as the activation energy E_μ of the charge-carrier mobility ($E_\sigma = E_\mu + E_n$), we determined both activation energies as well (Arrhenius plots are shown in Fig. S5 of the Supplemental Material [47]) and depicted all of them again as a function of the maximum annealing temperature T_{max} in Fig. 5. Again, the initial run (black circles) and the second run after the flush with synthetic air (red diamonds) are shown. In Fig. 5(a) the activation energy E_σ of the electrical conductivity starts in the first run above 300 meV

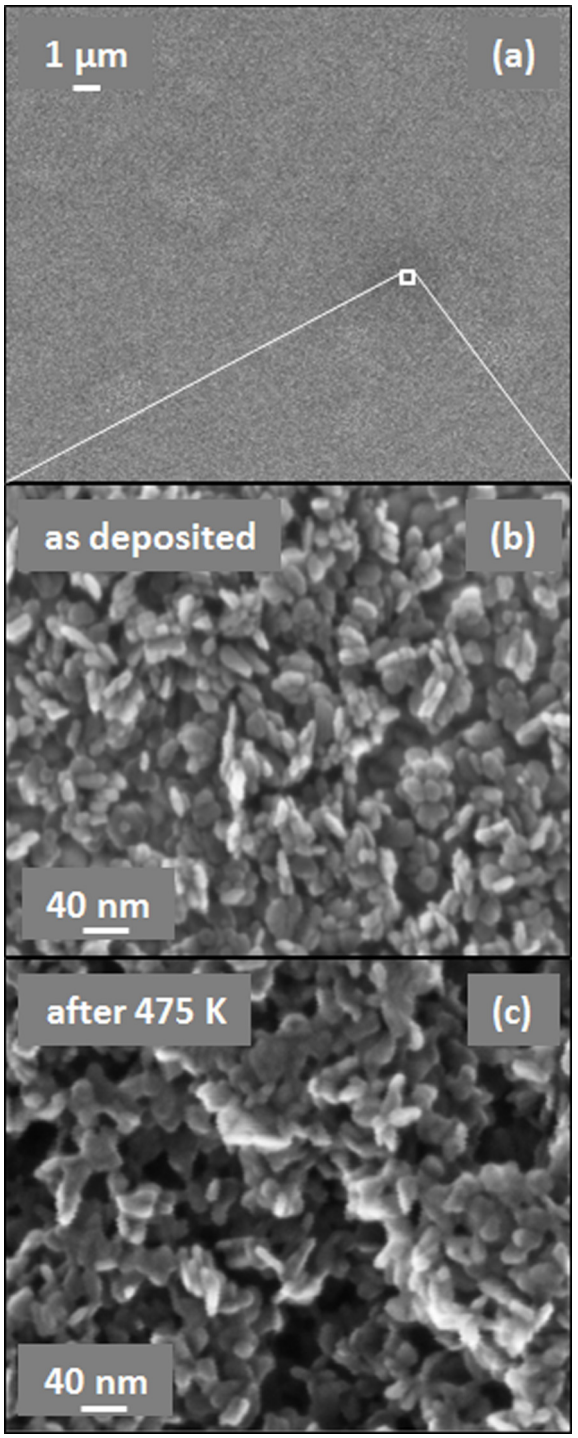

FIG. 4. Scanning electron microscopy (SEM) images of ligand-exchanged Bi_2S_3 nanoparticles. (a) Overview and (b) zoom after deposition and (c) after annealing up to 475 K.

and decreases within the temperature regions I and II down to around 180 meV in region III. In Fig. 5(b) the uncertainty of the determined activation energy E_μ of the carrier mobility is visible by the depicted error bars.

However, as indicated by the dashed black line in Fig. 5(b), the activation energy of the mobility decreases from ~125 meV down to around 30 meV during the first run. As expected from the consistency of the activation energies

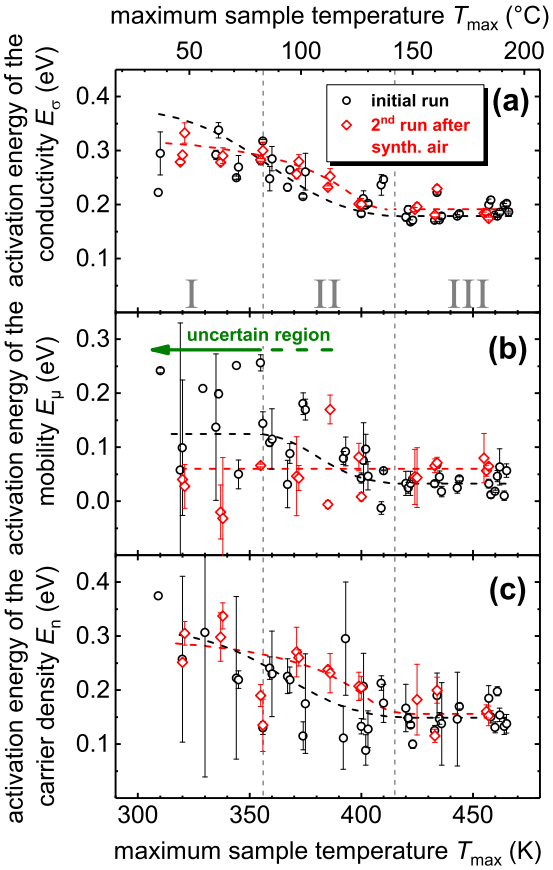

FIG. 5. The activation energies derived from the Arrhenius plots (a) of the electrical conductivity, (b) the charge-carrier mobility, and (c) the charge-carrier density as a function of the maximum annealing temperature T_{max}. The experimental routine is the same as performed in Fig. 3. The vertical lines separate different temperature regions mentioned in the text.

($E_\sigma = E_\mu + E_n$), the activation energy E_n of the charge-carrier density [Fig. 5(c)] decreases also from around 300 meV down to around 150 meV during the first run. So, we conclude from the first run that the increase of the charge-carrier mobility by two orders of magnitude [see Fig. 3(b)] is linked to a decrease of the activation energy of the mobility. We attribute this decrease to a reduced potential barrier the charge carriers have to overcome during transport. This explanation agrees with the observation of a sintered nanoparticle layer after temperature treatment.

At this point we want to add that no literature references for the activation energy of the mobility for Bi_2S_3 (as nanoparticles or bulk material) have been published yet to our knowledge.

To comment on the sign of the determined activation energies we have to point out that our calculation of the charge-carrier density and mobility from the measured thermoelectric powers is based on an assumed dominant scattering mechanism at (localized) ionized defects (see also Sec. II C). The central point is that we can describe the carrier transport limited by potential fluctuations in the conduction band. The model makes no assumption about the types of these defects, e.g., whether they exist as native point defects or as surface defects. In particular we picture the interface areas of the

nanoparticles as severe potential fluctuations, which pose a barrier for the carrier transport (correlated to E_μ). During annealing these potential fluctuations are reduced, resulting in lower values for E_μ and higher absolute mobilities. Unfortunately, our investigated temperature range is too small to precisely determine the temperature dependence of the mobility (which is expected to be $\propto T^{3/2}$ for the ionized defect scattering model [57,58]), so we can speculate about the alternative explanation that the carrier transport is limited by a hopping process between the nanoparticles, which would explain the activated carrier mobility as well [59]. However, this model should not hold for the sintered nanoparticle layers after annealing, and discontinuities in the mobility data would be expected.

Furthermore, we qualitatively attribute the activation energy of the charge-carrier density to the distance of the Fermi energy to the conduction band edge, which decreases while introducing sulfur vacancy donors.

As stated before, the sintering process of the nanoparticle layer is irreversible during the flush with synthetic air. Thus, the activation energy of the carrier mobility remains constant within the uncertainties of the measurements in Fig. 5(b) during the second run (red diamonds). But the value of E_μ equates to around 60 meV, which is 30 meV above the end of the first run. One possible explanation is that the introduced oxygen atoms affect the potential barrier and therefore cause the shifted activation energy of the mobility.

However, the atmospheric flush passivates the sulfur vacancy donors with oxygen and therefore reduces the charge-carrier density, while in the second run (in vacuum) after the flush, the charge-carrier density rises again by around two orders of magnitude, which is again consistent with the reduced activation energy of the charge-carrier density [red diamonds in Fig. 5(c)].

Now we want to focus on the energetic position of the vacancies that cause the n-type doping of the Bi_2S_3 nanoparticle layer. As calculated recently by Tumelero *et al.* for Bi_2S_3 bulk material [41], the energetic distance of the vacancies to the conduction band edge is at least 0.42 eV. Thus, the question rises, is it possible to gain charge-carrier densities of up to 3×10^{18} cm^{-3} by such (deep) doping states? Therefore, we want to estimate the overall concentration of (neutral and ionized) vacancies N_D that is necessary for this charge-carrier concentration. The number of ionized donors per cubic centimeter is given by [60,61]

$$N_D^+ = \frac{N_D}{1 + 2\exp\left(\frac{E_F - E_D}{kT}\right)}, \tag{6}$$

where E_D is the energetic distance of the donor state with respect to the vacuum energy, N_D is the overall concentration of donors (neutral and ionized), and N_D^+ is the number of ionized donors. If we now assume that the charge-carrier density is equal to the number of ionized donors ($n = N_D^+$) and express the charge-carrier density by the Boltzmann approximation (which is applicable for $n \leqslant 0.1 N_C \approx 10^{18}$ cm^{-3}), we obtain

$$n(T) = N_C(T)\exp\left(\frac{E_F - E_C}{kT}\right). \tag{7}$$

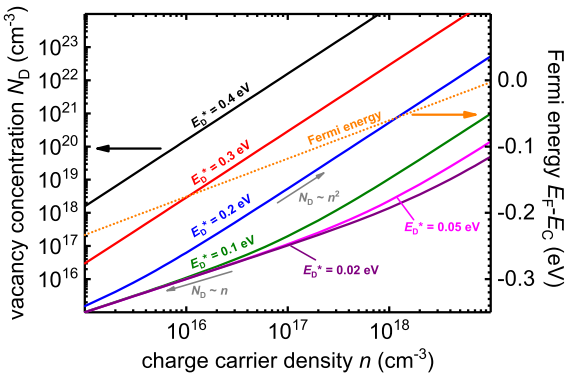

FIG. 6. Calculation of the (neutral and ionized) vacancy concentration N_D [see Eq. (3)] as a function of the charge-carrier density n, that is assumed to be equal to the concentration of ionized vacancies ($n = N_D^+$), for different energetic distances E_D^* of the doping vacancy to the conduction band edge. The right y axis depicts the position of the Fermi energy (orange dots) in reference to the conduction band edge (via the Boltzmann approximation). The dominant proportionality of Eq. (3) is marked with gray arrows. The used effective density of states is $N_C = 1.13 \times 10^{19}$ cm^{-3}.

Solving Eq. (7) for E_F and inserting the Fermi energy in Eq. (6), we obtain

$$N_D = n + 2\frac{n^2}{N_C}\exp\left(\frac{E_D^*}{kT}\right), \tag{8}$$

where E_D^* is the energetic distance of the donor state with respect to the conduction band edge. In Fig. 6 we show the calculated vacancy concentration N_D as a function of the charge-carrier density (the ionized vacancies) for several energetic positions E_D^* of the vacancy states relative to the conduction band edge (between 0.02 eV and 0.4 eV at room temperature). The dominant proportionalities are marked with gray arrows, and the Fermi energy from the Boltzmann approximation is also plotted as orange dots. We observe that for $E_D^* = 0.4$ eV (black line) the necessary vacancy concentration N_D is above 10^{24} cm^{-3} for $n = 10^{18}$ cm^{-3}, which is too high to be physically possible.

The molar mass of bismuth sulfide bulk material (514 g/mol) and the mass density (6.78 g/cm^3) correspond to a concentration of 7.9×10^{21} Bi_2S_3 molecules per cubic centimeter. Thus, with $E_D^* = 0.4$ eV and $n = 10^{17}$ cm^{-3} already every bismuth sulfide molecule would exhibit one sulfur vacancy (Bi_2S_2). Therefore, the energetic distance of the dopants has to be below 0.4 eV. Thus, we derive from this approximation that either the energetic distance from the donors to the conduction band edge was well overrated by Tumelero *et al.*, or the energetic positions of the donors at the surface (or near the surface) of bismuth sulfide are different from those of the bulk.

Therefore, we want to estimate a plausible energetic position of the doping sulfur vacancies. The stoichiometry of $Bi_2S_{2.9}$ (one out of ten molecules exhibits a sulfur vacancy) would correspond to a vacancy concentration of $N_D \approx 8 \times 10^{20}$ cm^{-3}, which corresponds to $E_D^* < 0.2$ eV for $n > 10^{18}$ cm^{-3}. For a stoichiometry of $Bi_2S_{2.99}$ the vacancy concentration would equal $N_D \approx 8 \times 10^{19}$ cm^{-3}, corresponding

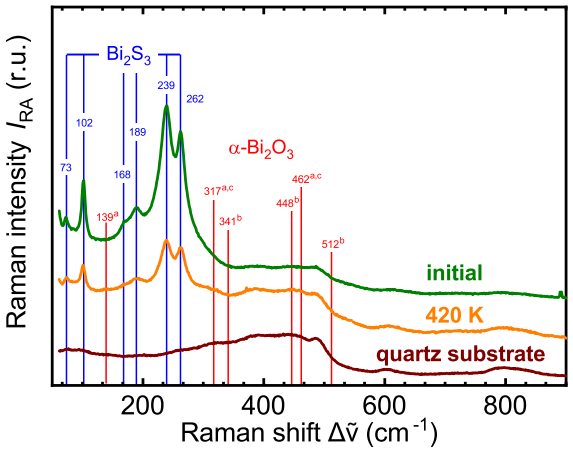

FIG. 7. Raman spectroscopy of pristine bismuth sulfide nanoparticles (green line) and after annealing under vacuum conditions up to a temperature of 420 K (orange line). The background of the quartz glass substrate is depicted in brown. The Raman measurements were performed under ambient conditions. Expected Raman modes for bismuth sulfide taken from literature are marked by vertical blue lines [63,64]. Raman modes of bismuth oxide, which are not visible in the spectra—even after annealing up to 420 K in vacuum and exposing the sample to lab atmosphere at room temperature—are marked by vertical red lines (a [65], b [66], c [67]).

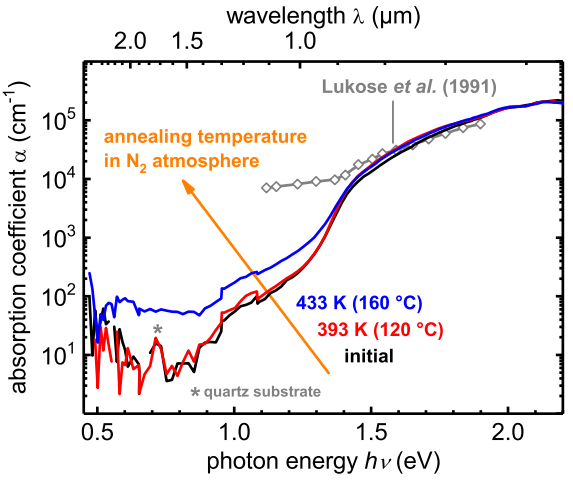

FIG. 8. Optical absorption coefficient as a function of the photon energy determined with photothermal deflection spectroscopy (PDS) for three bismuth sulfide nanoparticles samples, which were annealed with different temperatures under nitrogen atmosphere. The absorption coefficient of bismuth sulfide by Lukose *et al.* is depicted with gray diamonds [52]. The strong deviation of this reference and our results especially for energies below 1.5 eV is due to a higher dynamic range of the PDS method. After annealing the sample up to 433 K a significantly enhanced absorption of photons with energies below the optical band gap of bismuth sulfide is observed.

to $E_D^* \approx 0.1$ eV for $n \approx 3 \times 10^{18}$ cm^{-3}. Thus, assuming that between one and ten percent of the bismuth sulfide molecules exhibit a sulfur deficiency, the energetic distance (E_D^*) of the doping sulfur vacancies to the conduction band edge should be smaller than 0.2 eV.

In this context, we want to interpret the observed saturation of the charge-carrier density [$n = 3 \times 10^{18}$ cm^{-3} in temperature region III in Fig. 3(b)] as a maximal stoichiometric deviation that bismuth sulfide can exhibit. If so, the above-mentioned slightly smaller maximal charge-carrier density of the second run ($n = 2 \times 10^{18}$ cm^{-3} after the flush with synthetic air) could be due to a decreased maximal sulfur vacancy concentration. This reduced maximal sulfur vacancy concentration is therefore due to the oxidized bismuth sulfide ($Bi_2S_{3-x}O_x$) directly after the air flush. So, we found that during the second run (i.e., stepwise thermal annealing) not all of the oxygen atoms leave the bismuth sulfide and therefore reduce the maximal sulfur vacancy concentration. This interpretation is supported by the known higher binding energy of bismuth oxide (α-Bi_2O_3) compared to bismuth sulfide [62].

To support our conclusion that the doping vacancy states are significantly more shallow than 0.4 eV, we present Raman spectroscopy measurements. In Fig. 7 Raman measurements are shown of the same bismuth sulfide nanoparticle sample directly after the deposition (initial, green) and after annealing up to 420 K (orange) under a vacuum base pressure of 10^{-6} mbar in the thermopower setup. In addition, a reference Raman measurement of a cleaned quartz glass substrate is given (brown). Expected Raman modes for bismuth sulfide (from Refs. [63,64]) are marked by vertical blue lines, whereas expected Raman modes for bismuth oxide (α-Bi_2O_3; Refs. [65–67]) are marked by vertical red lines. Both before and after the temperature treatment the characteristic Raman modes for bismuth sulfide (especially at 73, 102, 168, 189, 239, and 262 cm^{-1}) are detectable. In contrast, Raman modes of bismuth oxide are not detectable.

However, if the amount of oxidized bismuth sulfide molecules ($Bi_2S_{3-x}O_x$, $x \approx 0.1$) were equal to ten percent (as mentioned above), and if the Raman cross sections of bismuth sulfide were comparable to the cross sections of bismuth oxide, Raman modes for bismuth oxides would be detectable. Therefore, we doubt that oxidized bismuth sulfide exhibits stable Raman modes of bismuth oxide or that the amount of oxidized molecules is as high as ten percent, which would correspond to an energetic distance E_D^* of the doping states around 0.2 eV as calculated in the previous section. If the doping vacancies are as shallow as 0.1 eV, the amount of oxidized bismuth sulfide molecules would be around one percent. But, we assume that such a low amount of bismuth oxide is below the detection limit of Raman spectroscopy. Thus, the Raman measurements support our argument that the doping by sulfur vacancies results from states which are shallower than 0.2 eV.

A more sensitive optical measurement is the determination of the absorption coefficient via photothermal deflection spectroscopy (PDS), which features a dynamic range of several orders of magnitude. In Fig. 8 the absorption coefficients of three bismuth sulfide nanoparticle samples are depicted. The samples were annealed at different temperatures under nitrogen atmosphere (H_2O and $O_2 < 1$ ppm, which corresponds to an oxygen partial pressure that is comparable to a vacuum base pressure below 10^{-3} mbar). The absorption coefficient was calculated including an effective layer thickness, which was estimated based on Lukose *et al.* [52] (gray diamonds in Fig. 8).

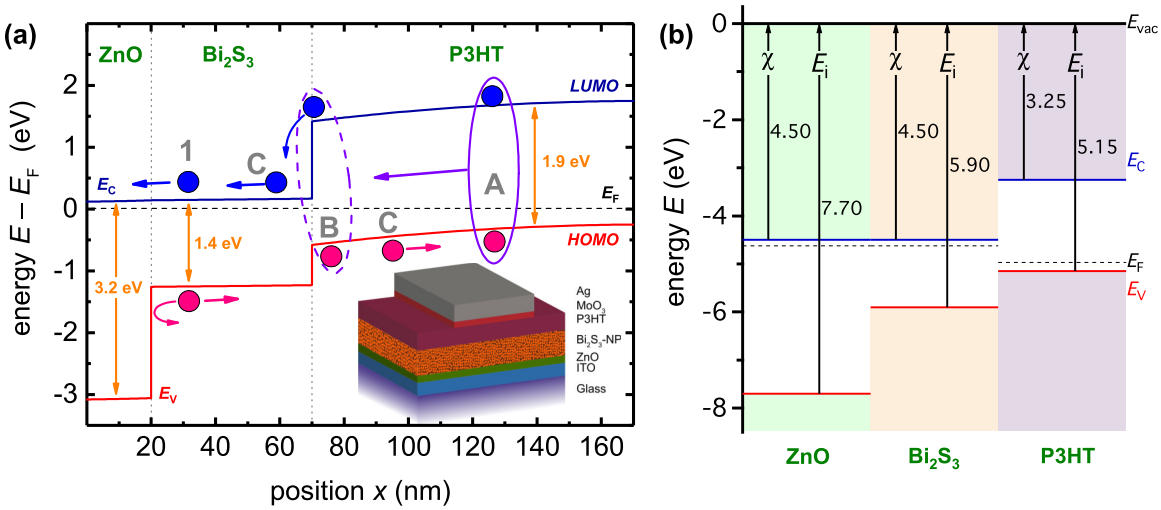

FIG. 9. Schematic band diagram of the active part of a planar (bulk layer) solar cell (ZnO/Bi_2S_3/P3HT) referenced to the Fermi level (a). In principle, photogeneration takes place within the bismuth sulfide (labeled as 1) and within P3HT (labeled as A). Photogenerated charge carriers within the P3HT layer occur as excitons (depicted as violet oval), which diffuse toward the heterojunction interface, where they dissociate (labeled as B). Afterward, the charge carriers diffuse toward the outer contacts of the device (labels C). Inset: Schematic drawing of the planar layer stack of the heterojunction hybrid solar cell. An energy level diagram of the unconnected layers with respect to the vacuum level is shown in (b) with χ and E_i marking the electron affinity and ionization energy, respectively. Used values for ZnO are from [73,74], for Bi_2S_3 from [17,75], and for P3HT from [76].

The absorption coefficient of the pristine nanoparticle layer (black line in Fig. 8) increases by two orders of magnitude between 1.2 eV and 1.5 eV, which is attributed to the fundamental absorption over the optical band gap of bismuth sulfide. Below 1.2 eV the sub-band-gap absorption takes place, whereas the characteristic peak at 0.72 eV is due to absorption within the quartz glass substrate (labeled by *). Sub-band-gap absorption mainly occurs by the following two mechanisms: On one hand occupied (defect) states within the band gap can be excited over the conduction band edge and on the other hand electrons can be excited from the valence band into unoccupied states within the band gap. Therefore, we attribute a higher absorption coefficient for photon energies below the optical band gap (<1.4 eV) to an increased density of (defect) states within the band gap. The sample, which was annealed at a temperature of 393 K (red line), shows sub-band-gap absorption comparable to the pristine sample. However, a higher annealing temperature of 433 K (blue line) leads to a significantly increased absorption below 1.4 eV. Therefore, this increased absorption corresponds to a higher density of defect states that we attribute to a rising sulfur deficiency of the bismuth sulfide nanoparticles. It is worth mentioning here that although PDS is a highly sensitive optical method, optical measurements to determine the sulfur deficiency of bismuth sulfide are still not as sensitive as electrical measurements.

B. Bi_2S_3/P3HT solar cells

While the conductivity and thermopower measurements discussed above allowed a detailed assessment of majority carrier-transport properties, for the use in solar cells also minority carrier properties of Bi_2S_3 are of great importance, as their transport can be the bottleneck in the device. Therefore, we fabricated planar heterojunction solar cells with the layer stack glass/ITO (120 nm)/ZnO (50 nm)/Bi_2S_3 ($2 \times$ DLE $\cong$ 50 nm)/poly(3-hexylthiophene-2,5-diyl) (P3HT) (80 nm)/MoO_x (30 nm)/Ag (200 nm) as shown in the inset of Fig. 9. To illustrate the band alignment between ZnO, Bi_2S_3, and P3HT, a schematic band diagram is shown in Fig. 9(a). Besides the photogenerated charge carriers in the Bi_2S_3 layer (labeled as 1), excitons are generated in the P3HT layer (label A). These excitons diffuse (within several nanometers) toward the Bi_2S_3/P3HT interface, where they dissociate (label B). Subsequently the separated charge carriers travel toward the respective contacts (label C).

In order to understand the contribution of the Bi_2S_3 and the P3HT to the photocurrent, we performed spectrally resolved measurements of photocurrent and absorptance. Fourier transform photocurrent spectroscopy (FTPS) was used to study the photocurrent of Bi_2S_3/P3HT solar cells and P3HT-only reference cells and photothermal deflection spectroscopy (PDS) was used to obtain the absorptance of P3HT and Bi_2S_3 thin films. Figure 10 shows the result of these FTPS and PDS measurements as a function of photon energy (lower x axis) or wavelength (upper x axis). The data shown as the solid orange line represent the spectral photocurrent of the full Bi_2S_3/P3HT device stack as shown in the inset of Fig. 9(a), while the dashed orange line only refers to a device with P3HT but without Bi_2S_3. The blue lines represent the absorption coefficient α of Bi_2S_3 (solid) and of P3HT (dashed). To determine absolute values of the quantum efficiency, FTPS spectra were calibrated according to the method section. The commonly used form for EQE results (linear scaling as a function of the wavelength λ) is depicted in Fig. S6 of the Supplemental Material [47], showing maximum quantum efficiencies of around 12% for the Bi_2S_3/P3HT devices and 10% for the ZnO/P3HT reference devices.

The data show that for photon energies $E > 1.9$ eV (roughly corresponding to $\lambda < 650$ nm), P3HT absorbs

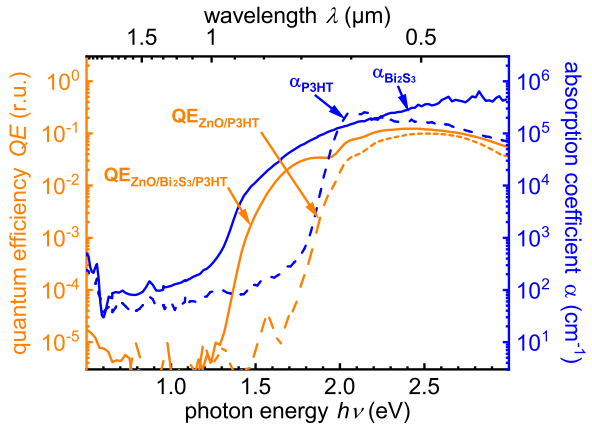

FIG. 10. Quantum efficiency QE (left axis) determined with FTPS of a bismuth sulfide nanoparticle solar cell (solid orange line) and a ZnO/P3HT reference cell without nanoparticles (dashed orange line) as a function of photon energy. The absorption coefficient α (right axis) of a bismuth sulfide nanoparticle layer is depicted as solid blue line and of a P3HT layer as a dashed blue line. Below the optical band gap of P3HT (around 1.9 eV) and above the band gap of Bi_2S_3 (around 1.4 eV) the nanoparticle solar cell exhibits significant enhancement in quantum efficiency.

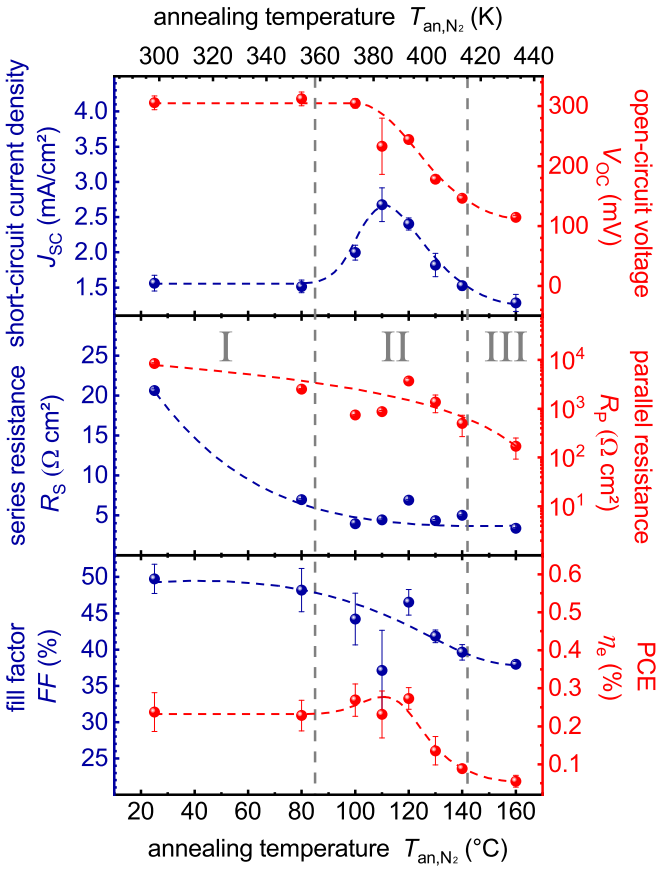

FIG. 11. Device performance parameters of bismuth sulfide nanoparticle solar cells extracted from *I-V* measurements as a function of the annealing temperature of the nanoparticle layer. The annealing was performed under nitrogen atmosphere before the P3HT layer was deposited. The determined temperature regions I–III from the electrical transport studies are depicted as vertical dashed gray lines. The error bars indicate the standard deviation of the average value within six solar cells processed on one substrate.

comparably to Bi_2S_3 and therefore contributes to the photocurrent of the planar heterojunction device in this energy range. For lower photon energies, $1.3 < E < 1.9$ eV, the Bi_2S_3 layer is the only possible source of photocurrent. By comparison between the photocurrent of the Bi_2S_3/P3HT device compared to the P3HT-only device, we see that there is a clearly visible contribution to the photocurrent also from Bi_2S_3. However, the quantum efficiency in the range $1.3 < E < 1.9$ eV is substantially reduced relative to the quantum efficiency at higher photon energies, where P3HT dominates.

In the following, we will have a look at the main solar cell parameters as a function of annealing temperature of the Bi_2S_3 layer depicted in Fig. 11 (plotted in °C on the lower x axis and in K on the upper x axis). These parameters were deduced from *I-V* measurements carried out in the dark and under illumination, which are depicted in Fig. S7 of the Supplemental Material [47]. The annealing was performed under nitrogen atmosphere before the P3HT layer was deposited. In addition to the power conversion efficiency η_e, the fill factor FF, the short-circuit current density J_{SC} and the open-circuit voltage V_{OC}, we also determined series and parallel resistances (details given in the methods section). We also indicated the regions I, II, and III used earlier in the discussion of Figs. 3 and 5. Except for the reduction of the series resistance, there is little change in region I. In region II, i.e., for annealing temperatures $360 < T < 415$ K, J_{SC} has a peak, while the V_{OC} starts to decrease continuously. The decrease of V_{OC} as a function of annealing temperature is most likely correlated with the increase of charge-carrier concentration, which likely coincides with a decrease of charge-carrier lifetime, which we will discuss later. To judge the effect of the Bi_2S_3 layer on the solar cell performance, *I-V* characteristics of reference ZnO/P3HT cells are shown in Fig. S7 as well. These cells produced only very low photocurrents around 0.5 mA/cm^2 and efficiencies around 0.1% as result of the reduced absorption compared to the Bi_2S_3/P3HT devices. These results are comparable to the work by other groups reporting also quite low efficiencies for ZnO/P3HT bilayer devices [68–71].

In Fig. 12 we show FTPS measurements of the annealed solar cell series. In Fig. 12(a) the quantum efficiency QE is depicted as a function of the photon energy. It can be seen that with rising annealing temperature the contribution of photogenerated charge carriers with photon energies smaller than the optical band gap of bismuth sulfide (straight orange arrow) also rises. Therefore, the introduction of sulfur vacancy defect states within the optical band gap contributes to the short-circuit current density. More relevant for J_{SC} is the QE enhancement for photon energies above 1.4 eV. For photon energies above the optical band gap of P3HT (around 1.9 eV) the QE exhibits a maximum in dependency of the annealing temperature (round orange arrow). To depict the trend of QE we plotted the quantum efficiency as a function of the annealing temperature in Fig. 12(b) for several photon energies (open symbols). Here, the mentioned trends above are clearer: Below 1.4 eV the QE is enhanced almost continuously with rising annealing temperature. An increase in the near-infrared

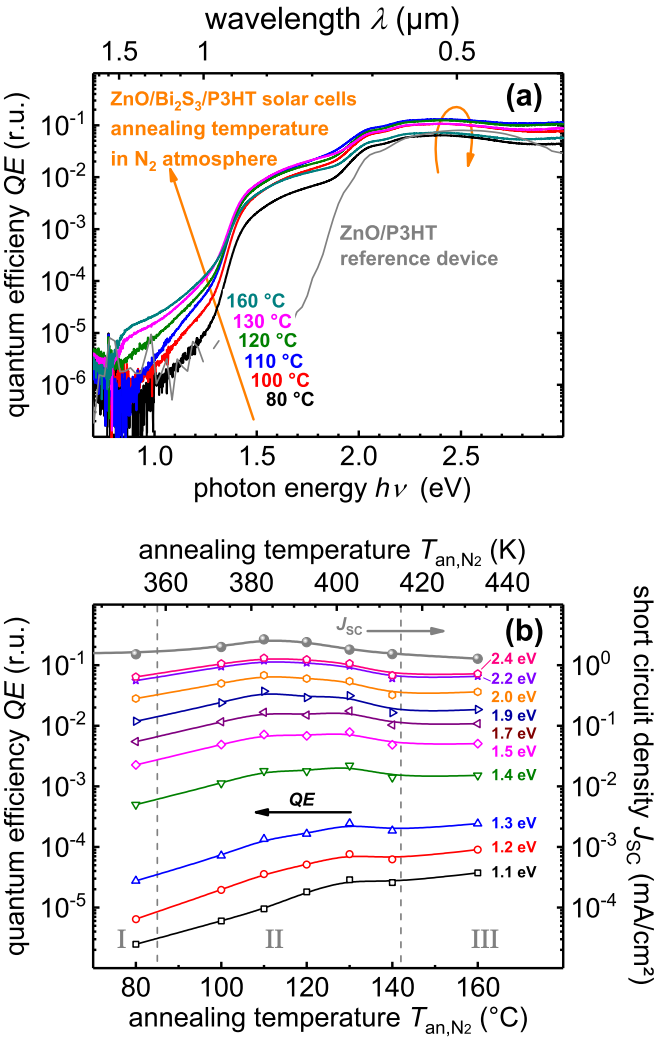

FIG. 12. (a) Quantum efficiency QE of the solar cell annealing series (see Fig. 10) determined with FTPS as a function of the photon energy. (b) Quantum efficiency at certain photon energies as a function of the annealing temperature. The short-circuit density J_{SC} (right y axis) of the device illuminated with white light is depicted with gray dots.

photoresponse for sulfur-deficient Bi_2S_3 has recently been demonstrated and explained by the contribution of in-gap states [72].

Between photon energies from 1.4 eV to 1.9 eV, the maximum of the quantum efficiency shifts from 130 °C down to 110 °C. For photon energies of 1.9 eV and above, the QE exhibits the same trend observed in Fig. 11 for the short-circuit density with a maximum at 110 °C. So we plotted J_{SC} for comparison on the right y axis. Because both photoactive layers, bismuth sulfide and P3HT, contribute to the photocurrent in this spectral range, it is ambiguous which mechanism dominates the enhancement of J_{SC}. The following effects will combine: With higher annealing temperature photogenerated excitons in the P3HT dissociate better at the interface with Bi_2S_3 and the electron transport within the Bi_2S_3 is enhanced, which raises the contribution of the polymer. Additionally, because of the reduced potential barriers within the Bi_2S_3 nanoparticle layer (as discussed in Sec. III A) also the charge-carrier transport toward the P3HT of photogenerated holes (minorities) is enhanced with rising annealing temperature, which can increase the contribution of the nanoparticle layer to the short-circuit current.

However, the drastically decreasing open-circuit voltage within the second temperature region and the lowered short-circuit density for annealing temperatures higher than 110 °C indicate that a new loss channel in the solar cell becomes active. In order to identify this additional loss channel, we determined the dark-current density J_0 via fitting the dark I-V curves to the diode equation without illumination (details in the method section). We interpret J_0 as a quantitative value for the amount of recombination losses in the solar cell in the dark [53]. The dependence of the dark-current density on the annealing temperature depicted in Fig. 13(a) as blue dots (left y axis) is of special interest. J_0 rises around three orders of magnitude within the annealing-temperature range.

To combine the solar cell results with our transport studies on annealed bismuth sulfide nanoparticle layers, we also plotted the charge-carrier density from Fig. 3 which rises around 2.5 orders of magnitude (red dots) on the right y axis in Fig. 13(a). Thus, we observe a strong correlation between the introduced (ionized) sulfur vacancies of the annealed nanoparticle layer and the dark-current density of the solar cell. We expect the loss mechanism in the solar cell to originate from recombination of charge carriers via (ionized and neutral) defect states within the band gap (Shockley-Read-Hall recombination). As mentioned in the electrical transport part of this paper, the number of ionized sulfur vacancies ($N_D^+ \approx n$) can be significantly smaller than the total amount of introduced (neutral) sulfur vacancies N_D, mainly depending on the energetic position E_D^* of the vacancy. Therefore, we want to use our previous result depicted in Fig. 6 (N_D as a function of n for several energetic positions E_D^*) to determine the concentration of the vacancies, i.e., the proposed recombination centers. The required charge-carrier density can be obtained from Fig. 13(a) assuming that the annealing temperature for the cell, $T_{an,N2}$, is close to the respective temperature T_{max} in the film. This allows us to use use $J_0(T_{an,N2})$ and $n(T_{max})$ to derive $J_0(n)$.

The result is combined with the data of the derived vacancy concentration in Fig. 13(b). Here the dark-current density is depicted as blue dots on the left y axis and the calculated $N_D(n, E_D^*)$ is depicted again as solid colored lines on the right y axis. We found the best agreement of the trend for $J_0(n > 10^{17}\ \mathrm{cm}^{-3})$ with $N_D(E_D^* \simeq 0.05\text{–}0.1\ \mathrm{eV})$. This again supports our conclusion that in the present nanoparticle-based samples the sulfur vacancies are significantly shallower than stated by Tumelero *et al.* for bulk Bi_2S_3 (bulk: $E_D^* > 0.4$ eV). Furthermore, we can conclude that excessive doping with sulfur vacancies is detrimental for the solar cell in terms of introducing high concentrations of defect states within the band gap and therefore drastically enhances the recombination losses.

However, we also showed that the annealing of the bismuth sulfide nanoparticle layer is beneficial for the short-circuit current density and therefore for the overall efficiency of the solar cell up to an annealing temperature of 110 °C. We believe that the enhancement of the charge-carrier mobility by two orders of magnitude in the sintered nanoparticle layer is

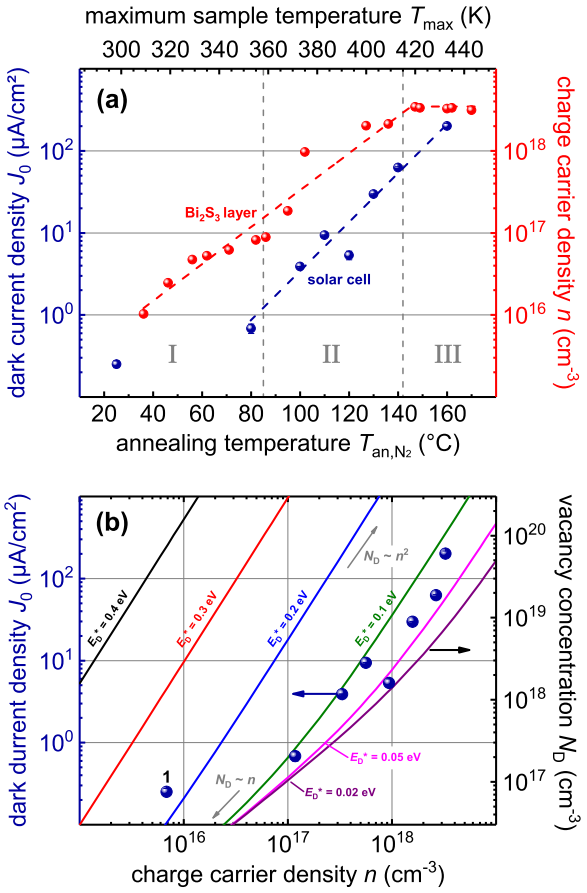

FIG. 13. (a) Dark-current density J_0 (left axis) determined from fitting Eq. (5) to the *I-V* measurements of the solar cell series as a function of the annealing temperature $T_{an,N2}$ (lower x axis). The charge-carrier density (right y axis) of the nanoparticle layer determined via thermopower measurements (see Fig. 3) is depicted with red dots as a function of the maximum sample temperature T_{max} (upper x axis). We assign to each value of $J_0(T_{an,N2})$ an interpolated value of $n(T_{max})$ with the assumption of $T_{max} = T_{an,N2}$ and thereby plot $J_0(n)$ in (b) as blue dots (left y axis). Additionally, we plot our calculation of the (neutral and ionized) vacancy concentration N_D for several energetic positions E_D^* (colored lines) of the vacancies in respect to the conduction band edge (from Fig. 6) on the right y axis again as a function of the charge-carrier concentration. Thereby, we correlate the significantly increased dark-current density of the solar cells with the approximated defect density of the sulfur-deficient bismuth sulfide nanoparticle layer. We find the best agreement of this correlation with E_D^* in the range between 0.05 eV and 0.1 eV.

the dominant reason for the enhanced solar cell performance. Thus, to achieve an enhanced mobility without a drastically rising dark-current density, we expect that an annealing step with a successive passivation of the crucial high defect density (e.g., sulfur treatment) can be a promising procedure to enhance the overall solar cell performance.

IV. CONCLUSION

In the first part of this work we performed a detailed study on the enhanced transport properties of bismuth sulfide nanoparticle layers during moderate temperature annealing (300–480 K) in vacuum. By annealing, we improved the electrical conductivity by more than four orders of magnitude. In order to identify the reasons for the enhanced conductivity, we perform thermoelectric power measurements that allow us to distinguish between an enhancement of the charge-carrier mobility by two orders of magnitude caused by sintered nanoparticles and an increase in charge-carrier density by more than two orders of magnitude caused by sulfur vacancies in off-stoichiometric bismuth sulfide (Bi_2S_{3-x} with $x > 0$). We discussed the energetic position of the sulfur vacancies that act as electron donors. Thereby, we state that these donors in nanoparticle layers are significantly shallower than expected from the literature for bulk material.

In the second part, we applied the thermal treatment (vacancy doping) to the bismuth sulfide nanoparticle layer which was then used in combination with P3HT as an organic-inorganic planar heterojunction solar cell. Thereby, we showed that the annealing of the nanoparticle layer is beneficial for the solar cell performance up to a temperature of 383 K (110 °C), which we attribute mainly to the enhanced charge-carrier mobility within the nanoparticle layers. For higher annealing temperatures we observed a drastically reduced open-circuit voltage that we correlate with an increase in the dark current density by three orders of magnitude. Thereby, we conclude that too many introduced sulfur vacancies increase recombination of charge carriers through (native point) defect states within the band gap of bismuth sulfide.

ACKNOWLEDGMENTS

This work was partially funded by the German Federal Ministry of Education and Research (BMBF) Project No. 03SF0402A, "NADNuM." The authors would like to thank Oliver Thimm and Josef Klomfaß (FZJ) for the PDS measurements and Markus Hülsbeck (FZJ) for kind support with the Raman spectroscopy.

[1] Y. Zhou, M. Eck, and M. Krüger, Energy Environ. Sci. **3**, 1851 (2010).
[2] G. Chen, J. Seo, C. Yang, and P. N. Prasad, Chem. Soc. Rev. **42**, 8304 (2013).
[3] J. Duan, H. Zhang, Q. Tang, B. He, and L. Yu, J. Mater. Chem. A **3**, 17497 (2015).
[4] M. V. Kovalenko, L. Manna, A. Cabot, Z. Hens, D. V. Talapin, C. R. Kagan, V. I. Klimov, A. L. Rogach, P. Reiss, and D. J. Milliron *et al.*, ACS Nano **9**, 1012 (2015).
[5] M. Bernechea, N. C. Miller, G. Xercavins, D. So, A. Stavrinadis, and G. Konstantatos, Nat. Photonics **10**, 521 (2016).
[6] S. D. Stranks and H. J. Snaith, Nat. Nanotechnol. **10**, 391 (2015).
[7] W. Zhang, G. E. Eperon, and H. J. Snaith, Nat. Energy **1**, 16048 (2016).
[8] G. Niu, X. Guo, and L. Wang, J. Mater. Chem. A **3**, 8970 (2015).

[9] N. H. Tiep, Z. Ku, and H. J. Fan, Adv. Energy Mater. **6**, 1501420 (2016).

[10] B. Conings, J. Drijkoningen, N. Gauquelin, A. Babayigit, J. D'Haen, L. D'Olieslaeger, A. Ethirajan, J. Verbeeck, J. Manca, E. Mosconi, F. D. Angelis, and H.-G. Boyen, Adv. Energy Mater. **5**, 1500477 (2015).

[11] D. Wang, M. Wright, N. K. Elumalai, and A. Uddin, Sol. Energy Mater. Sol. Cells **147**, 255 (2016).

[12] A. Babayigit, D. Duy Thanh, A. Ethirajan, J. Manca, M. Muller, H.-G. Boyen, and B. Conings, Sci. Rep. **6**, 18721 (2016).

[13] A. Babayigit, A. Ethirajan, M. Muller, and B. Conings, Nat. Mater. **15**, 247 (2016).

[14] I. J. Kramer and E. H. Sargent, Chem. Rev. **114**, 863 (2013).

[15] M. Yuan, M. Liu, and E. H. Sargent, Nat. Energy **1**, 16016 (2016).

[16] C.-H. M. Chuang, P. R. Brown, V. Bulović, and M. G. Bawendi, Nat. Mater. **13**, 796 (2014).

[17] A. K. Rath, M. Bernechea, L. Martinez, and G. Konstantatos, Adv. Mater. **23**, 3712 (2011).

[18] A. K. Rath, M. Bernechea, L. Martinez, F. P. G. de Arquer, J. Osmond, and G. Konstantatos, Nat. Photonics **6**, 529 (2012).

[19] L. Martinez, M. Bernechea, F. de Arquer, and G. Konstantatos, Adv. Energy Mater. **1**, 1029 (2011).

[20] L. Martinez, A. Stavrinadis, S. Higuchi, S. L. Diedenhofen, M. Bernechea, K. Tajima, and G. Konstantatos, Phys. Chem. Chem. Phys. **15**, 5482 (2013).

[21] M. Bernechea, Y. Cao, and G. Konstantatos, J. Mater. Chem. A **3**, 20642 (2015).

[22] A. J. MacLachlan, F. T. O'Mahony, A. L. Sudlow, M. S. Hill, K. C. Molloy, J. Nelson, and S. A. Haque, ChemPhysChem **15**, 1019 (2014).

[23] L. Whittaker-Brooks, J. Gao, A. K. Hailey, C. R. Thomas, N. Yao, and Y.-L. Loo, J. Mater. Chem. C **3**, 2686 (2015).

[24] R. Mohan, Nat. Chem. **2**, 336 (2010).

[25] J. Liu, X. Zheng, L. Yan, L. Zhou, G. Tian, W. Yin, L. Wang, Y. Liu, Z. Hu, Z. Gu, C. Chen, and Y. Zhao, ACS Nano **9**, 696 (2015).

[26] L. Martinez, S. Higuchi, A. J. MacLachlan, A. Stavrinadis, N. C. Miller, S. L. Diedenhofen, M. Bernechea, S. Sweetnam, J. Nelson, and S. A. Haque *et al.*, Nanoscale **6**, 10018 (2014).

[27] J. Black, E. M. Conwell, L. Seigle, and C. W. Spencer, J. Phys. Chem. Solids **2**, 240 (1957).

[28] P. Larson, V. A. Greanya, W. C. Tonjes, R. Liu, S. D. Mahanti, and C. G. Olson, Phys. Rev. B **65**, 085108 (2002).

[29] J. Mock, B. Klingebiel, F. Köhler, M. Nuys, J. Flohre, S. Muthmann, T. Kirchartz, and R. Carius, Phys. Rev. Mater. **1**, 065407 (2017).

[30] G. Wang, Y. Ling, and Y. Li, Nanoscale **4**, 6682 (2012).

[31] G. Wang, Y. Yang, D. Han, and Y. Li, Nano Today **13**, 23 (2017).

[32] Y. Bekenstein, K. Vinokurov, S. Keren-Zur, I. Hadar, Y. Schilt, U. Raviv, O. Millo, and U. Banin, Nano Lett. **14**, 1349 (2014).

[33] B. Chen, C. Uher, L. Iordanidis, and M. G. Kanatzidis, Chem. Mater. **9**, 1655 (1997).

[34] H. Mizoguchi, H. Hosono, N. Ueda, and H. Kawazoe, J. Appl. Phys. **78**, 1376 (1995).

[35] K. Biswas, L.-D. Zhao, and M. G. Kanatzidis, Adv. Energy Mater. **2**, 634 (2012).

[36] Z.-H. Ge, B.-P. Zhang, P.-P. Shang, and J.-F. Li, J. Mater. Chem. **21**, 9194 (2011).

[37] Z.-H. Ge, B.-P. Zhang, Z.-X. Yu, and J.-F. Li, J. Mater. Res. **26**, 2711 (2011).

[38] A. D. Schricker, M. B. Sigman, Jr., and B. A. Korgel, Nanotechnology **16**, S508 (2005).

[39] S.-C. Liufu, L.-D. Chen, Q. Yao, and C.-F. Wang, Appl. Phys. Lett. **90**, 112106 (2007).

[40] Q. Han, J. Chen, X. Yang, L. Lu, and X. Wang, J. Phys. Chem. C **111**, 14072 (2007).

[41] M. A. Tumelero, R. Faccio, and A. A. Pasa, J. Phys. Chem. C **120**, 1390 (2016).

[42] R. Chmielowski, D. Péré, C. Bera, I. Opahle, W. Xie, S. Jacob, F. Capet, P. Roussel, A. Weidenkaff, G. K. H. Madsen, and G. Dennler, J. Appl. Phys. **117**, 125103 (2015).

[43] D. Guo, C. Hu, and C. Zhang, Mater. Res. Bull. **48**, 1984 (2013).

[44] L. Martínez Montblanch, The *n*-type bismuth sulfide coloidal nanocrystals and their application to solution-processed photovoltaic devices, Ph.D. thesis, Universitat Politècnica de Catalunya, 2014.

[45] D. J. Riley, J. P. Waggett, and K. G. U. Wijayantha, J. Mater. Chem. **14**, 704 (2004).

[46] M. Aresti, M. Saba, R. Piras, D. Marongiu, G. Mula, F. Quochi, A. Mura, C. Cannas, M. Mureddu, A. Ardu, G. Ennas, V. Calzia, A. Mattoni, A. Musinu, and G. Bongiovanni, Adv. Funct. Mater. **24**, 3341 (2014).

[47] See Supplemental Material at http://link.aps.org/supplemental/10.1103/PhysRevMaterials.3.105406 for results obtained for single ligand exchanged nanoparticles, schematic drawings of the experimental setups, full thermopower data, Arrhenius plots for n and μ, I-V data for the solar cells, and linearly scaled QE data.

[48] W. Beyer and H. Overhof, Semicond. Semimetals **21**, 257 (1984).

[49] J. Y. W. Seto, J. Appl. Phys. **46**, 5247 (1975).

[50] A. C. Boccara, D. Fournier, W. Jackson, and N. M. Amer, Opt. Lett. **5**, 377 (1980).

[51] W. B. Jackson, N. M. Amer, A. C. Boccara, and D. Fournier, Appl. Opt. **20**, 1333 (1981).

[52] J. Lukose and B. Pradeep, Solid State Commun. **78**, 535 (1991).

[53] J. Nelson, *The Physics of Solar Cells* (Imperial College Press, London, 2003).

[54] T. C. M. Müller and T. Kirchartz, in *Advanced Characterization Techniques for Thin Film Solar Cells*, edited by D. Abou-Ras, T. Kirchartz, and U. Rau (Wiley-VCH Verlag, 2016), pp. 189–214.

[55] A. C. Glatz and V. F. Meikleham, J. Electrochem. Soc. **110**, 1231 (1963).

[56] Q. Yang, C. Hu, S. Wang, Y. Xi, and K. Zhang, J. Phys. Chem. C **117**, 5515 (2013).

[57] E. Conwell and V. F. Weisskopf, Phys. Rev. **77**, 388 (1950).

[58] H. Brooks, Adv. Electron. Electron Phys. **7**, 85 (1955).

[59] P. Guyot-Sionnest, J. Phys. Chem. Lett. **3**, 1169 (2012).

[60] S. M. Sze and K. K. Ng, *Physics of Semiconductor Devices* (John Wiley & Sons, 2006).

[61] W. Shockley, *Electrons and Holes in Semiconductors* (D. Van Nostrand Company, Inc., Toronto, 1953).

[62] W. E. Morgan, W. J. Stec, and J. R. Van Wazer, Inorg. Chem. **12**, 953 (1973).

[63] Y. Zhao, K. T. E. Chua, C. K. Gan, J. Zhang, B. Peng, Z. Peng, and Q. Xiong, Phys. Rev. B **84**, 205330 (2011).
[64] I. Zumeta-Dubé, J.-L. Ortiz-Quiñonez, D. Díaz, C. Trallero-Giner, and V.-F. Ruiz-Ruiz, J. Phys. Chem. C **118**, 30244 (2014).
[65] F. D. Hardcastle and I. E. Wachs, J. Solid State Chem. **97**, 319 (1992).
[66] S. N. Narang, N. D. Patel, and V. B. Kartha, J. Mol. Struct. **327**, 221 (1994).
[67] A. J. Salazar-Pérez, M. A. Camacho-López, R. A. Morales-Luckie, V. Sánchez-Mendieta, F. Ureña-Núñez, and J. Arenas-Alatorre, Superf. Vacío **18**, 4 (2005).
[68] D. C. Olson, S. E. Shaheen, M. S. White, W. J. Mitchell, M. F. A. M. van Hest, R. T. Collins, and D. S. Ginley, Adv. Funct. Mater. **17**, 264 (2007).
[69] J.-M. Chiu and Y. Tai, ACS Appl. Mater. Interfaces **5**, 6946 (2013).
[70] A. Pickett, A. Mohapatra, A. Laudari, S. Khanra, T. Ram, S. Patil, and S. Guha, Org. Electron. **45**, 115 (2017).
[71] K. P. Musselman, S. Albert-Seifried, R. L. Z. Hoye, A. Sadhanala, D. Muñoz-Rojas, J. L. MacManus-Driscoll, and R. H. Friend, Adv. Funct. Mater. **24**, 3562 (2014).
[72] N. Huo, A. Figueroba, Y. Yang, S. Christodoulou, A. Stavrinadis, C. Magén, and G. Konstantatos, Adv. Opt. Mater. **7**, 1900258 (2019).
[73] K. Jacobi, G. Zwicker, and A. Gutmann, Surf. Sci. **141**, 109 (1984).
[74] B.-K. Na, M. A. Vannice, and A. B. Walters, Phys. Rev. B **46**, 12266 (1992).
[75] H. Moreno-García, M. T. S. Nair, and P. K. Nair, Thin Solid Films **519**, 2287 (2011).
[76] J. C. Nolasco, R. Cabré, J. Ferré-Borrull, L. F. Marsal, M. Estrada, and J. Pallarès, J. Appl. Phys. **107**, 044505 (2010).